

RESEARCH ARTICLE OPEN ACCESS

Bacterial Expression of Gene-Encoding DNA Origami Structures

Verena Dobretzberger^{1,2}  | Alexander Hebel³ | Maria Ponetsmüller³ | Florian Ohner¹ | Trishant R. Umrekar⁴  | Morgan Beeby⁴ | Friedrich C. Simmel³ | Ivan Barišić^{1,5} 

¹Molecular Diagnostics, Centre for Health and Bioresources, AIT Austrian Institute of Technology GmbH, Vienna, Austria | ²Faculty of Technical Chemistry, Technical University Vienna, Vienna, Austria | ³Department of Bioscience, TUM School of Natural Sciences, Technical University Munich, Garching, Germany | ⁴Department of Life Science, Imperial College London, London, UK | ⁵Eko Refugium d.o.o., Slunj, Croatia

Correspondence: Ivan Barišić (Ivan.Barisic@ait.ac.at)

Received: 27 November 2025 | **Revised:** 19 December 2025 | **Accepted:** 5 January 2026

Keywords: bacterial expression | DNA-based data storage | DNA origami | DNA uptake | gene delivery

ABSTRACT

Previous studies have shown that DNA origamis assembled from gene-encoding scaffolds can be taken up by mammalian cells and ultimately lead to the expression of the encoded genes. While interactions of DNA origami structures with mammalian cells have been extensively investigated, their interactions with bacteria remain poorly understood. Here, we systematically study how structure, folding state, chemical functionalization, and polycationic coatings influence the uptake and expression of gene-encoding DNA origami structures in *E. coli*. Using complementary positive- and negative selection assays, we show that DNA origami structures display markedly lower transformation efficiencies than their corresponding circular single-stranded scaffolds. Folding geometry, compactness, and scaffold accessibility strongly modulate transformation, with partially folded origami structures showing considerably higher activity. Chemical functionalization did not improve uptake, whereas polyplex formation can improve stability and transformation. Fluorescence and electron microscopy reveal that DNA origami structures predominantly associate with the bacterial surface. Leveraging the intrinsically low transformability of intact DNA origamis, we engineered photocleavable nanostructures that enable UV-triggered release of gene-encoding scaffolds, providing switchable activation of transformation. Our results offer fundamental insights into the bacterial processing of DNA nanostructures and establish a framework for controlling DNA entry and expression using programmable nanoscale carriers.

1 | Introduction

DNA is best known as the genetic blueprint of life, yet its structural programmability enables it to serve as an exceptional nanoscale building material. The DNA origami technique enables the folding of defined 2D or 3D nanostructures through a self-assembly process, in which a long single-stranded scaffold is combined with hundreds of short staple oligonucleotides to create a designed DNA architecture [1, 2]. In recent years, there has been increasing interest in the use of DNA origami constructs in biomedical applications. In this context, it has been demonstrated that genetically encoded DNA origami in combination with mimicry of cellular

components has great potential for gene therapy [3, 4]. Consequently, there has been a lot of investigative effort in interactions of DNA origami with eukaryotic cells and potential. However, little has been studied regarding the interaction between bacteria and DNA origami, with only a few exceptions [5, 6]. DNA origami structures were used as biosensors for bacteria [7] or as antimicrobial devices [8]. These DNA constructs could offer a platform for controlled antimicrobial drug delivery, providing target specificity, reduced side effects, and improved stability. Furthermore, DNA origami structures are appealing as cargo themselves. They may serve as vehicles for genetic information

Verena Dobretzberger, Alexander Hebel, and Maria Ponetsmüller contributed equally to this study.

This is an open access article under the terms of the [Creative Commons Attribution](https://creativecommons.org/licenses/by/4.0/) License, which permits use, distribution and reproduction in any medium, provided the original work is properly cited.

© 2026 The Author(s). *Small Structures* published by Wiley-VCH GmbH.

or other DNA-encoded data contained within the scaffold [9]. After uptake, bacteria can retrieve, copy, store, and read the encoded information using their inherent genetic machinery.

Previous studies have demonstrated successful delivery and expression of gene-encoding DNA origami structures in mammalian cells [10–12]. In the present work, we explore how DNA origami structures and tailored modifications mediate interactions with and uptake by bacteria. To address this, we conducted experiments exploiting diverse DNA origami structures for functional uptake and expression in *E. coli*. The specifics of the DNA origami architecture (e.g., bundle vs. wireframe technique, helix number, and crossover spacing) allows for tuning of the overall size, shape, and mechanical properties of the structures, thereby influencing downstream biological processes [13, 14], and potential interactions with the target bacteria. DNA origami with densely packed helices might be less accessible to the genetic machinery but can be functionalized more precisely to mediate specific interactions with the cell surface. Therefore, we also conducted experiments with DNA origami modified with biotin (Bt) or antimicrobial peptide (AMP), attempting to leverage the unique properties of these molecules to associate with and cross the membrane. Other biotinylated molecules have been previously shown to associate non-specifically or covalently with the *E. coli* surface and in some cases even enter the cell [15]. Regarding AMPs, their strategic deployment may localize DNA origami to bacteria rather than killing them, a principle that echoes concepts such as vancomycin-modified DNA origami targeting bacteria [8]. AMPs, although less specific than ligands such as aptamers, are robust under a wide range of environmental conditions and can be produced without requiring complex synthetic procedures [16].

Apart from DNA origami functionalization, their overall stability in physiological media is crucial for successful targeting of bacteria. Origami stability is affected primarily by insufficient ionic screening under low-salt conditions, nuclease activity, and non-specific protein adsorption [17]. To counteract unfavorable environmental conditions, multivalent cations have been shown to exert beneficial stabilizing effects [18–21]. When cationic polymers interact with DNA, they form polyplexes, which can protect against nucleolytic degradation and facilitate the delivery of genetic material into cells [22, 23]. To account for the experimental and culture conditions relevant to bacteria, we employed PEI-25 kDa, PEI-40 kDa, and chitosan to enhance the structural stability and membrane permeability [24–26].

In this study, we dissect how DNA origami architecture and chemical functionalization influence their interactions with *E. coli* and the uptake and expression of their genetic payload. To benchmark these synthetic structures against the single-stranded circular scaffold, we established complementary transformation assays based on positive and negative selection systems.

2 | Results

2.1 | Transformation of DNA Origami Structures

To examine the interaction of gene-encoding DNA origami structures with *E. coli* cells, we evaluated two different experimental setups. A heat shock transformation was performed followed by a selection process unique to each assay. For positive selection, DNA origami structures were assembled from scaffolds encoding

an antibiotic resistance marker and a fluorescent reporter protein. Transformed cells were plated on antibiotic-containing agar, and resistant colonies were quantified as colony-forming units (CFU) (Figure 1A). In a second, negative selection assay, DNA origami structures were assembled from scaffolds encoding M13 bacteriophages. Following transformation, infected cells produced clear plaques on a bacterial lawn, quantified as plaque-forming units (PFU) (Figure 1B).

The origami structures used here were deliberately chosen because they represent robust, high-yield designs that cover two widely used construction principles—compact bundle-based objects and a more open wireframe architecture. Different architectures impart distinct physicochemical properties, while remaining compatible with the same scaffold-encoded payload. This provides a consistent platform to link architecture to uptake and express outcomes.

For the first set of experiments, we produced a 4549-nt circular single-stranded scaffold (CSS) that carries, as a defined payload, a carbenicillin-resistance marker and a contiguous sequence encoding green fluorescent protein (GFP) together with its promoter from the coding (sense) direction of the corresponding plasmid (Section S4.1). Two different DNA origami structures were assembled from this scaffold. The first design is a rigid 20-helix bundle (HB: $82 \times 13 \times 10$ nm) with a dense square lattice, created in caDNAo [27]. Single-stranded DNA handles were placed at defined positions to enable site-specific attachment of fluorophores for optical readout. The second design is a wireframe octahedron (Oct: $38 \times 38 \times 38$ nm) defined by eight six-HB edges, designed using the Athena software [28] and further adjusted to our scaffold length in caDNAo (Figure 2A and Section S4.1). Because all three inputs—CSS, HB, and Oct—derive from the same DNA sequence encoding both the carbenicillin-resistance cassette and the GFP expression unit, and experiments were conducted at matching molar concentrations, the resulting colonies allow a direct comparison of transformation efficiencies. The 3D structures of the origami designs were validated in silico using oxView [24]. Representative transmission electron microscopy (TEM) micrographs of the assembled and purified structures are shown in Figure 2B.

Under the experimental conditions used, the raw mean colony count for transformation with CSS scaffold was 526 CFU, hence the transformation efficiency was determined to be 8.8×10^8 per nmol (Section S1.7). In contrast, the transformation efficiency using the DNA origami structures was markedly lower, corresponding to 3.2% for the HB and 2.3% for the Oct structure relative to the CSS scaffold. This indicates that successful transformation with DNA origami is a rare event (Figure 2C). Gel purification even further decreased the transformation efficiency of the DNA origami samples (Section S1.1). Comparable results were obtained for *E. coli* stored under different media conditions (Section S1.2).

For the second set of experiments, DNA origami architectures were assembled from M13mp18-derived scaffolds to enable negative selection. In total, five DNA origami structures were produced from three scaffold variants of 7249-nt, 7560-nt, and 8064-nt in length. Three of the designs—the nano bottle (NB; $25 \times 50 \times 25$ nm³, Sc7249) and two sheet-like structures (LS, RS; $40 \times 50 \times 15$ nm (Sc8064, Sc7560)—are multilayer architectures based on a honeycomb lattice. One square-lattice-based nanorod (Rod: 4×8350 nm, Sc8064) was chosen as an example of a highly elongated structure. Finally, we included a less

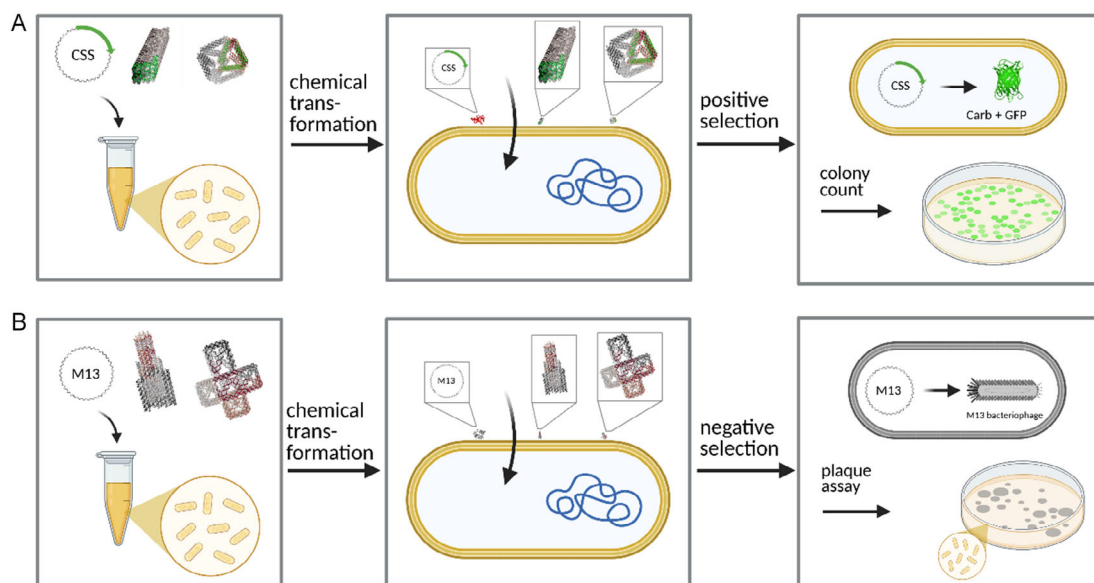


FIGURE 1 | Workflow for assessing DNA nanostructures targeting *E. coli* using positive and negative selection. Schematic representation of chemical transformation of *E. coli* with a circular single-stranded scaffold (CSS) and DNA origami nanostructures. Structures are drawn to scale to *E. coli* envelope in center panel. (A) Positive selection: Competent cells are individually transformed with the CSS or DNA origami, each supplied at equal molar concentration. Following recovery, cells are plated on carbenicillin-selective agar. Only cells that internalize and express the antibiotic-resistance cassette survive and additionally express GFP, enabling visual identification and quantitative colony counting. (B) Negative selection: *E. coli* XL-1 blue chemically competent cells sensitive to M13 are transformed with origami and scaffold DNA equivalent to method A. For selection, a plaque assay is performed by layer plating of cells mixed with semisolid agar. Upon expression of phage progenies, inhibition zones (plaques) appear as proof of transformation.

densely packed architecture folded using a wireframe routing strategy (WF: $40 \times 50 \times 40$ nm, Sc7560). All structures besides the WF, which was designed with the DAEDALUS software [29], were made using caDNAo. For the 3D structure in silico confirmation CATANA was used [30].

Because successful transformation of these M13-derived DNA origami architectures—or their corresponding single-stranded scaffolds—is expected to inhibit the growth of the host *E. coli* XL1-Blue strain, we conducted plaque assays for each origami structure and, in separate control experiments, for the respective scaffolds at equimolar concentrations. The experiments show that administration of the NB and WF structures to *E. coli* cultures led to plaque formation, indicating that the structures—or at least their underlying M13-based scaffolds—were taken up by the cells and expressed (Figure 2C). However, plaque formation remained very low, with the WF origami yielding on average only 4 PFU (0.2% of the value obtained with the corresponding scaffold alone) and the NB origami yielding 9 PFU (0.6% of the scaffold control). In the case of the WF structure, plaques were formed only after 5 h of regeneration, compared to 2.5 h for the NB. Within this experiment, the transformation efficiencies of the WF (7560-nt) and NB (7249-nt) scaffolds were calculated as 3×10^8 and 2.9×10^8 transformants per nmol, respectively. By contrast, the two similar LS and RS structures assembled from different scaffold size variants did not lead to observable *E. coli* transformation at all. Likewise, no PFU formation was observed with the long Rod structure. Differential analysis of the scaffold variants showed that the 7249-nt scaffold produced the highest transformation efficiency after 2.5 h regeneration, followed by the 8064-nt and 7560-nt scaffolds. After 5 h regeneration, PFU formation no longer differed between scaffold variants (Figure S6).

Overall, these results demonstrate that only a subset of DNA origami architectures can support measurable transformation. In both selection systems, the transformation efficiency of the gene-encoding origami structures remains markedly lower than that of the corresponding scaffolds. The observed structure- and scaffold-dependent differences suggest that the folding geometry and compactness of the origami structures play a decisive role in determining transformation outcomes.

2.2 | Impact of Folding State and Residual Scaffold on Transformation Efficiency

To elucidate the factors responsible for the reduced transformation efficiency of DNA origami compared to the pure scaffold, we conducted additional experiments using the HB structure. Because transformation experiments with gel-purified origami generally yielded lower efficiencies than PEG-purified samples (0.5% vs. 3.2% of the CSS transformation efficiency), we hypothesized that partially folded origami structures might transform more efficiently. For this reason, we deliberately folded DNA origami structures using incomplete sets of staple strands. Specifically, 25%, 50%, or 75% of the staples were added in the folding reaction, while the scaffold sequence and total DNA concentration were kept constant in all cases (Sections S1.3 and S4.1).

To assess the structural integrity of the HB origami structures folded with fewer staples, oxDNA simulations [27] were performed (Figure 3A). As the number of incorporated staples decreased, the simulated structures progressively lost their defined shape and became more conformationally flexible. Although the transformation efficiency increased from 3.0% (relative to CSS) as fewer staples were used, even the origami folded with the smallest staple

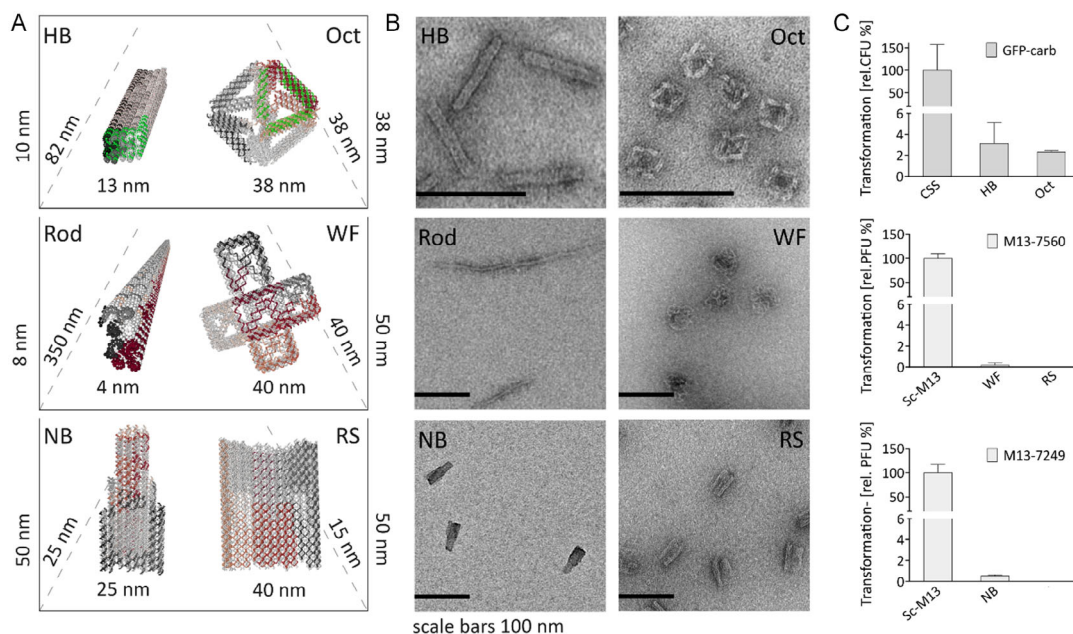


FIGURE 2 | Design, structural characterization, and *E. coli* transformation efficiency of DNA origami constructs. Top row: 20-helix bundle (HB) and wireframe octahedron (Oct) structures assembled from a 4549-nt scaffold encoding carbenicillin resistance and GFP (depicted in green). Middle and bottom rows: structures based on M13mp18 size variants for negative selection: nanorod 8064-nt (Rod), Daedalus wireframe 7560-nt (WF), nano bottle 7249-nt (NB), and right sheet-like structure 7560-nt (RS). Not depicted: left sheet-like (LS) origami, a structural equivalent to RS folded from the larger 8064-nt scaffold. (A) Monomeric 3D structures of gene-encoding DNA origami illustrated with CATANA. (B) Representative TEM micrographs showing correctly assembled and purified structures (scale bars: 100 nm). (C) Bar plot comparing transformation efficiency using equimolar scaffolds and origami structures. Relative values normalized to the scaffold and standard deviation (SD) shown for differential analyses of all data sets (CSS $n = 7$, HB/Oct $n = 3$, scaffold and M13-based origami $n = 2$). CFU counts after positive selection via carbenicillin and PFU counts after negative selection via growth inhibition zones are depicted.

set remained less efficient than pure CSS, reaching only 11.9% (Figure 3B).

We further hypothesized that spurious free scaffold present in the origami folding mixture (potentially remaining after purification) might be responsible for the observed transformation. To investigate the impact of residual scaffold after intended folding of an origami, we mixed intact HB origami with the corresponding CSS at defined molar fractions while keeping the total DNA concentration constant (Figure 3C). Even the addition of only 10% CSS markedly increased the transformation efficiency to 14.7% of the value obtained with pure CSS, and the effect became progressively stronger with higher scaffold fractions, reaching 66.7% upon addition of 75% CSS (Figure 3D).

2.3 | Transformation with Modified Biotin- and AMP–NB Structures

One of the major potential advantages of DNA origami structures compared to conventional gene vectors is the ability to functionalize them in a controlled manner—at defined locations and with defined stoichiometry. We therefore conducted additional experiments in which the NB structure was equipped with Bt or AMPs. Since Bt is an important cofactor for diverse bacterial metabolic processes, dedicated high affinity transport systems facilitate its uptake across the cytoplasmic membrane [31]. Previously, such transport systems were exploited to bypass the uptake size limits and transport Bt–peptide conjugates into the cell [15]. Following this example, we tested whether origami biotinylation enhances

transformation. Therefore, we assembled the NB structure with and without Bt-modified staples at five positions at the narrow end and compared plaque formation between both variants.

We observed that transformation with NB–Bt, which represents a relatively bulky conjugate, had no measurable effect on PFU formation compared to the unmodified NB (Figure 4C). In a second approach, a GF-17/oligonucleotide conjugate was hybridized via bridging strands to poly-T extensions protruding from the NB, yielding a NB-AMP construct carrying GF-17 at ten positions on the wide end of the structure. In a previous study, we demonstrated that the GF-17 AMP binds efficiently to *E. coli* but loses its antimicrobial activity if modified on the C-terminal end [32]. Given the size of the origami and the positioning of the AMPs, our aim was to promote proximity between the DNA and bacteria rather than to cause lethality. However, when NB–AMP was used in transformation experiments, PFU formation decreased by a factor of 50 relative to the nonfunctionalized NB (Figure 4C). This reduction may reflect interactions of the AMP moieties with the *E. coli* membrane that hinder translocation of the DNA into the cell. Although translocation impediment cannot be confirmed directly, our recent study on membrane binding of multiple AMP-functionalized origami structures (article in review) supports measurable membrane association.

2.4 | Transformation with NB Polyplexes

Subsequently, we assessed whether the stability and uptake of DNA origami can be enhanced using dedicated polymeric

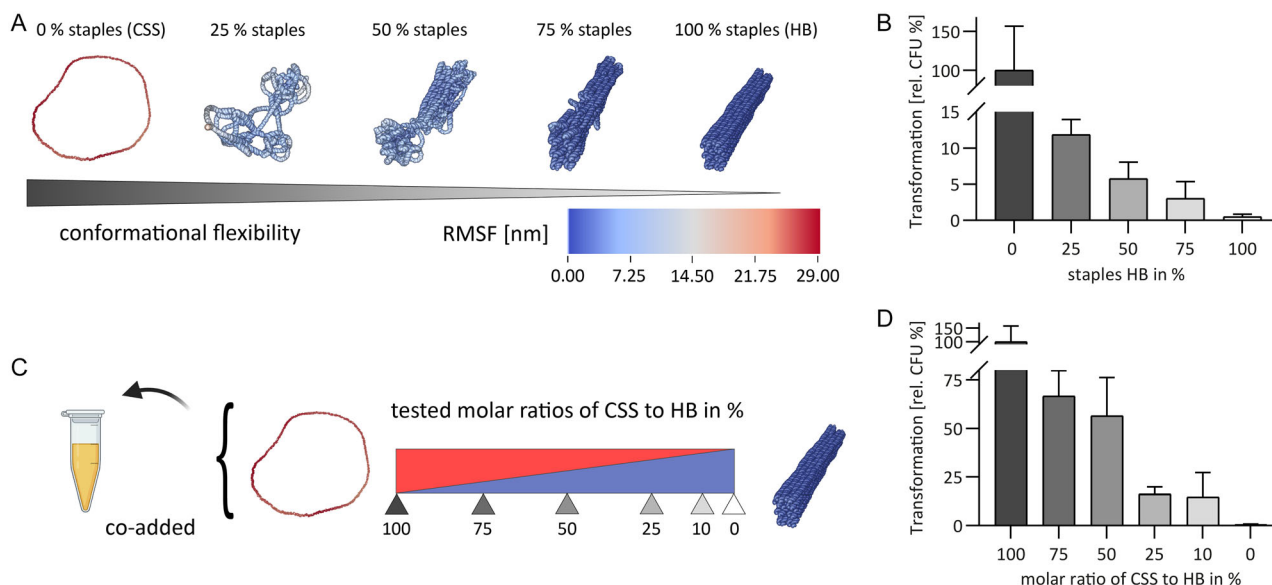


FIGURE 3 | Staple-saturation-dependent stability and scaffold-mixing effects on transformation efficiency. (A) oxDNA simulations illustrating the structural integrity of DNA origami folded with increasing staple numbers and of the single-stranded scaffold. Structures with 0% staples (CSS), 25% staples, 50% staples, 75% staples, and 100% staples (HB) of the full staple set were examined. As the number of staples increases, the simulated structures progressively gain their defined shape. (B) Transformation efficiencies with the corresponding origami variants normalized to the scaffold. A gradual decrease in transformation efficiency is observed with increasing staple numbers; however, even the most undersaturated origami (25% staples) exhibit lower efficiency than the pure scaffold. (C) Schematic Illustration of the scaffold-mixing assay. CSS and HB origami were combined at defined ratios, ranging from 100% to 0% CSS, while maintaining a constant total amount of DNA used for *E. coli* transformation. (D) Transformation efficiency with mixtures of intact origami (HB) and circular scaffold (CSS) at defined molar fractions, while keeping total DNA concentration constant. Even small additions of scaffold lead to a pronounced increase in transformation efficiency, which becomes more substantial with higher scaffold proportions. Relative values are normalized to the scaffold; error bars represent the standard deviation (SD). Data are based on $n = 7$ independent experiments for the scaffold and HB and $n = 3$ independent experiments for all other samples.

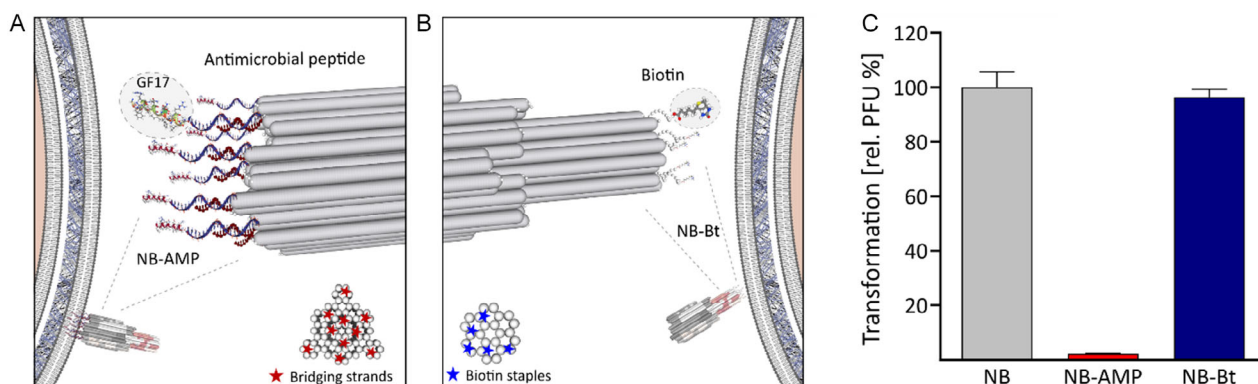


FIGURE 4 | Transformation of antimicrobial peptide (AMP) and biotin (Bt) modified NB structures. (A,B) Two different, modified NB structures in 1:1 scale with the *E. coli* membrane (small structures) are illustrated. The NB has a size of approx. $25 \times 50 \times 25$ nm in comparison to the Gram-negative bacterial envelope with approx. 40 nm thickness. Respective magnifications of modification sites are shown and were visualized using CATANA. (A) For the NB-AMP construct, GF17/oligonucleotide conjugates were hybridized to the wide end of the NB via complementary bridging strands at ten positions (honey comp red stars). (B) The second NB-Bt structure was functionalized via direct arrangement of Bt-staples during self-assembly at five positions of the narrow end (honey comp blue stars). (C) Bar plot of PFU formed after transforming *E. coli* with NB-AMP (red) and NB-Bt (blue) relative to the primary NB structure (gray). Mean PFU \pm SD relative to NB are shown ($n = 2$).

coatings. To this end, we formed polyplexes of the NB structure with the cationic polymers PEI-25 kDa, PEI-40 kDa, and chitosan. The specific molecular weights arise from the distinct monomeric subunits that assemble into the respective polymers. During polyplex formation, the positively charged monomers (number: N) bind electrostatically to the negatively charged

phosphates (number: P) of the DNA backbone. Hence, coating strength can be described by the N/P ratio.

In this experiment, N/P ratios between 0.03 and 8 were tested to evaluate their impact on the transformation efficiency. Based on our plaque assays, we found that, for all three polymers, coating improved PFU formation compared to uncoated NB up to an N/P

ratio of 0.5 (Figure 5). Above this threshold, however, transformation efficiency dropped sharply. Notably, this decrease was observed only for polymer-origami complexes and not for polyplexes formed with the scaffold alone (Figure 5). The best results were obtained with chitosan and PEI-25, which reached between 28% and 33% of the efficiency of the scaffold control.

We next investigated whether the transformation block observed at high N/P ratios arises because the gene-encoding DNA cargo is prevented from entering the cell, or whether inhibition occurs at a later stage by interfering with its expression. To address this question, we reproduced the first step of the M13 replication cycle—the formation of the double-stranded replicative form (RF)—to assess whether polymer addition alters expression-relevant processing. This was carried out by isothermal amplification using phi29 polymerase at 37°C, corresponding to the *E. coli* growth temperature. The results show that synthesis of the complementary strand becomes increasingly impeded with rising N/P ratios, with complete loss of replication occurring at an approximate threshold of $N/P \approx 2$ (Figure 5, heatmap). Although polymer-dependent reduction in polymerase accessibility or activity was evident, we cannot exclude that DNA-polymer complexes are also directly hindered at the membrane.

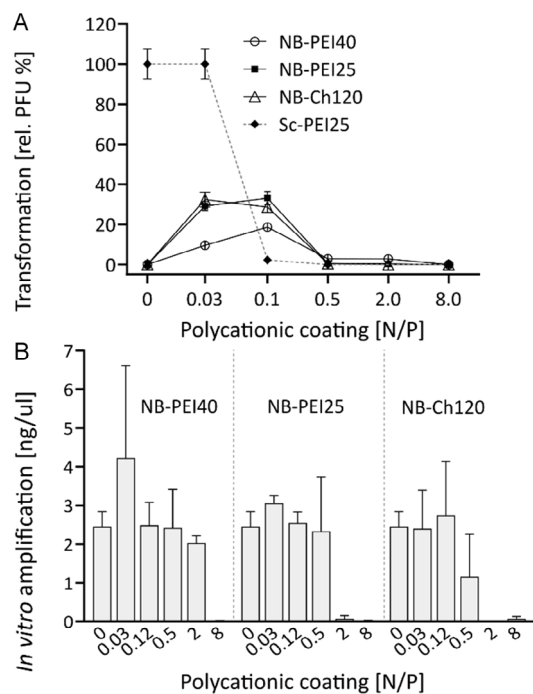


FIGURE 5 | Effect of NB-polyplexing on transformation. (A) NB structure polyplexes with increasing amounts of PEI-25 kDa, PEI-40 kDa, or chitosan 120 kDa at defined N/P ratios (N = cation and P = DNA monomer units). Mean PFU \pm SD relative to scaffold are shown. An optimum is observed between 0.03–0.5 N/P, above this threshold transformation is inhibited. PEI-scaffold polyplexes show a continuous decrease in PFU. PEI25-scaffold (Sc-PEI25) is shown representatively as a dotted line. (B) Bar plot of in vitro synthesized replicative form of M13 are depicted. NB-polyplexes were used as template for isothermal amplification and quantified via Qubit (ng/mL). Mean values \pm SD ($n = 2$) are given. Increasing N/P ratios progressively reduce amplification, leading to nearly abolished RF synthesis.

Additionally, to assess the effect of polycations on origami stability, we incubated NB-polyplexes and uncoated NB in *E. coli* culture supernatant (overnight culture, late phase). We then analyzed their stability after 1 day and after 1 week by agarose gel electrophoresis (AGE). As expected, the results show that NB-polyplexes exhibit markedly improved stability in the extracellular bacterial environment compared to uncoated NB structures (Figure S7).

The existence of an optimal N/P window for DNA origami polyplexes likely arises from a balance between partial charge neutralization, colloidal stability, and biological accessibility. Polyplex formation did not enhance transformation efficiency for the CSS alone, in contrast to the clear improvement observed for NB origami at low N/P ratios. Polyplex-mediated DNA delivery has primarily been developed for eukaryotic systems, where higher N/P ratios are commonly required and provide the additional benefit of facilitating endosomal escape [23, 33]. In bacteria, this mechanism is not required, and we therefore suggest that extensive polymer coating of the scaffold mainly necessitates an additional uncoating step, which can slow down replication and counteract potential gains.

2.5 | Localization of DNA Nanoparticles with *E. coli* Cells

To assess the interaction of DNA origami with bacterial cells in more detail, we imaged selected origami structures after incubating them in suspension with *E. coli*. For the HB nanostructure, we performed fluorescence microscopy as well as TEM, whereas for the NB structures we conducted cryo-electron tomography (cryo-ET) to assess interactions under native conditions.

For fluorescence imaging, HB origami structures were labeled with ATTO 647 fluorophores, which were attached to the origami surface via short staple extensions (Section S4.1). These labeled nanostructures were used in transformation experiments as described above and imaged after heat shock using an inverted fluorescence microscope (Nikon Ti2-E). Most observed *E. coli* cells exhibited a bright fluorescence signal (Figure 6A, top). Z-stack analysis showed that the signal was strongest at the cell periphery, indicating that the origami structures were associated with the bacterial surface (Video S1). The fluorescence appeared nonuniformly distributed across the surface, although individual origami structures could not be resolved due to the diffraction limit (Figure 6A, bottom).

To determine the position of the origami more precisely, an initial TEM screen was performed. Bacterial cells treated with either HB or Oct origami were placed on TEM grids and imaged using a FEI Tecnai T12 (120 kV). In both cases, the origami structures were found attached to the surface of the *E. coli* cells. For the HB structure, a slight aggregation at the bacterial surface was observed (Figure 6B), whereas the Oct appeared more evenly distributed (Figure 6C).

2.5.1 | DNA Uptake Kinetics and Cryo-ET of NB-Membrane Interactions

Fluorescence and TEM imaging demonstrated that DNA origami structures associate with the outer surface of *E. coli* cells, but these techniques cannot resolve whether or how the DNA crosses

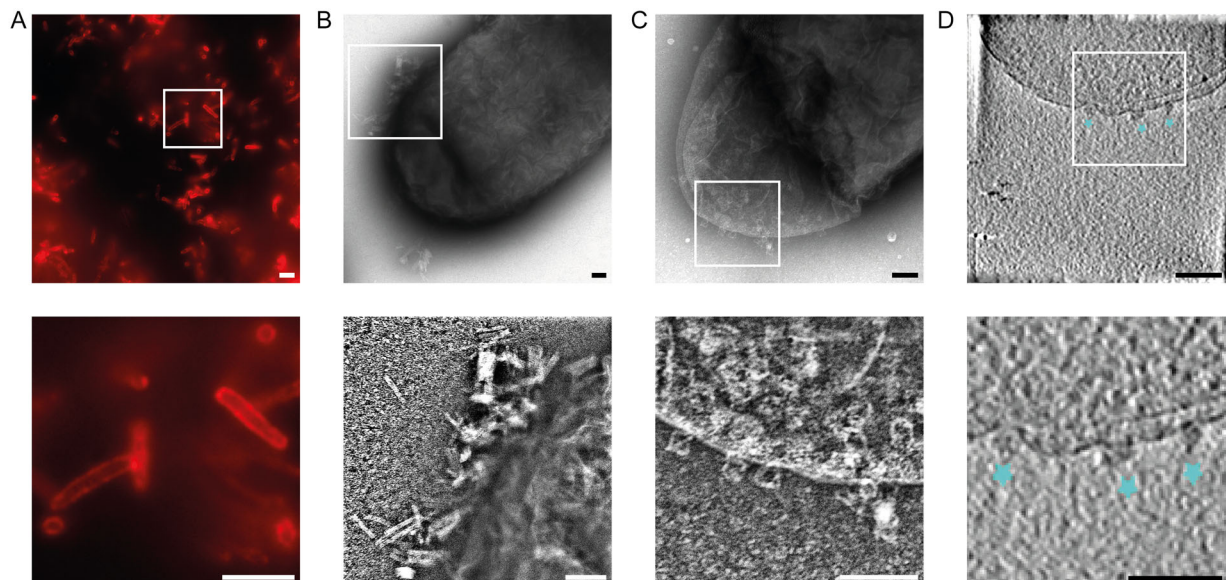


FIGURE 6 | Origami attachment to *E. coli* and assessment of cellular association using fluorescence microscopy, TEM, and Cryo-ET. (A) Top: Overview fluorescence image of *E. coli* transformed with ATTO 647-labeled HB. Most cells exhibit a bright fluorescence signal. Bottom: Zoom-in fluorescence image of the marked area. The fluorescence signal is concentrated at the cell periphery, indicating surface attachment of the origami structures; individual structures cannot be resolved due to the diffraction limit. (B) Top: TEM image of *E. coli* transformed with HB showing slight aggregation of origami at the cell surface. Bottom: Gaussian-filtered zoom-in. (C) Top: TEM image of *E. coli* transformed with octahedron (Oct) origami displaying a more uniform surface distribution. Bottom: Gaussian-filtered zoom-in. (D) Top: Cryo-ET image of *E. coli* XL1-Blue cells incubated with PEI25-nano bottle (NB) polyplex (N/P 0.1) revealing origami associated with the outer membrane. Bottom: zoom-in. NB origamis on the cell membrane have been marked with blue stars. Scalebars (A) 5 μm , (B–D) 100 nm.

the bacterial envelope. Because cryo-ET might allow visualization of the moment of membrane traversal, we sought to identify the most suitable experimental conditions to capture DNA “in flagranti”. To this end, and in preparation for cryo-ET imaging, we systematically examined the kinetics of heat-shock-mediated DNA uptake by reducing key steps of the standard transformation protocol (Table S1). Using the pMK4 shuttle vector to transform *E. coli* BL21, we first tested how rapidly DNA uptake occurs after adding DNA to chemically competent cells. We observed a remarkably fast process: incubation of only 2 s on ice is sufficient to promote DNA uptake by the majority of transformable cells, yielding 7×10^5 transformants/ml compared to 8×10^5 transformants/ml after the conventional 30-min incubation.

Next, we compared different cell aliquot volumes (5–75 μL). The number of transformants/ml varied from 6×10^5 in 75 μL to 5×10^6 in 5 μL , indicating that DNA adheres to the cells and is potentially taken up almost immediately upon contact. We further determined that the dedicated 42°C heat shock step can be omitted without reducing transformation efficiency. To verify these findings under imaging-compatible conditions, we repeated the kinetics assay using a “skinny” *E. coli* strain (*mreB* A125V) optimized for cryo-ET. Rapid transformation was also observed in this strain, although the efficiency was about 100-fold lower than in BL21.

Moving forward, we verified these conditions with the NB origami and scaffold control, respectively, showing similar PFU formation when the standard and optimized heat shock protocol was used. Finally, we used this protocol for in situ Cryo-ET preparations and further analysis of DNA uptake and localization. To obtain a detailed, near-native view of the interactions in the transformation context, native and competent *E. coli* cells with NB and PEI25-NB-polyplexes (0.1 N/P) were sampled for

Cryo-ET immediately after heat shock at RT. Both structures showed attachment to the cell surface of chemically competent *E. coli* (Figure 6D). Further images of this observations are depicted in Figure S8.

2.6 | DNA Release via a Photocleavable Origami Tether

Our transformation experiments described in the previous sections show that DNA origami structures are not superior to single-stranded scaffolds as gene vectors. The compact architecture of the origami seems to impede, rather than enhance, transformation and expression. Yet this drawback can be repurposed into an advantage: DNA nanostructures can serve as a controllable “transformation brake,” enabling precise regulation of when the genetic payload becomes accessible.

To leverage this capability, we designed photocleavable (PC) DNA structures by linking gene-encoding cargo to the nontransformable Rod via PC-bridge strands at six defined positions. As cargo, we used either the single-stranded scaffold (highly transformable but minimally addressable) or the NB structure (less efficient but precisely addressable), yielding the P-Sc and P-NB constructs, respectively. Upon UV irradiation at 365 nm, the PC-bridges are cleaved, releasing the DNA cargo for uptake (Figure 7D).

First, we verified the correct assembly of the P-structures using AGE. In the electrophoretic mobility-shift assay, the fully assembled constructs migrated with mobilities consistent with the expected size of the combined components, confirming successful formation of the final structures (Figure 7B). Furthermore, the assembly of the P-NB structure appears to be more efficient

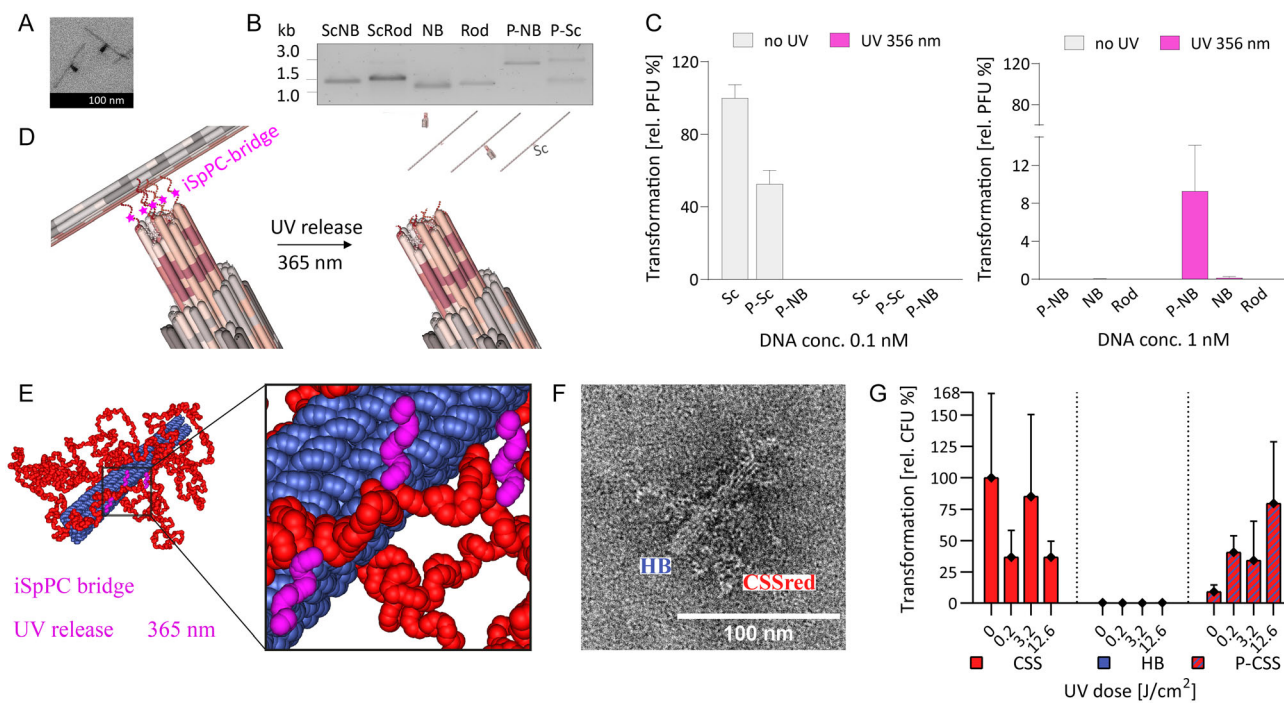


FIGURE 7 | Photocleavable (PC) DNA origami constructs. (A) TEM micrograph of the NB tethered to the Rod. (B) agarose gel electrophoresis of scaffolds (ScNB, ScRod) and respective origami (NB, Rod) including assembled PC structures (P-NB, P-Sc). Band of assembled PC structures appear at ~3 kb. Bands below indicate fractions of untethered DNA as seen in P-Sc at ~1.5 kb. (C) Bar plots showing mean PFU \pm SD ($n = 2$) relative to the scaffold after transformation with PC structures and single compounds before and after UV exposure with 2000 mJ/cm². (D) Schematic representation of the PC construct where the NB is tethered to the Rod via iSpPC-bridging strands (magenta). UV irradiation at 365 nm induces cleavage and release of the NB. (E) Schematic representation of the PC construct (P-CSS) where the circular scaffold (CSSred, red) is tethered to the helix bundle (HB, blue) via iSpPC-bridging strands (magenta) with zoom-in to the binding region. UV irradiation at 365 nm induces cleavage and release of the scaffold. (F) TEM micrograph of the assembled P-CSS showing the HB origami associated with the CSSred scaffold. (G) Bar plot comparing the relative transformation efficiencies using CSSred, HB, and the PC P-CSS across different UV doses. Data represent mean \pm SD from $n = 3$ independent experiments.

than that of the P-Sc, which is reflected by the ratio between the remaining lower band (unassembled components) and the higher bands (assembled product). This observation is consistent with our expectations, as the NB structure provides precise spatial addressability, which is not available with pure scaffold.

Next, we analyzed the UV-induced cleavage of the P-NB structures using doses between 150 mJ/cm² (~15 s) and 20 J/cm² (~1 h) via AGE. Cleavage was confirmed, as the bands corresponding to the PC-structure reverted to those of the separated components after UV exposure. The separation efficiency decreased continuously with lower UV doses (Figure S9).

Based on the AGE results, we performed transformation experiments with PC structures that were exposed to a UV dose of 2000 mJ/cm². Competent *E. coli* cells were thawed on ice and briefly centrifuged for 30 s at 2000 \times g before the DNA constructs were added. The reaction mixtures were irradiated with UV prior to continuing with the standard transformation protocol. We first tested the P-Sc and P-NB constructs and used the pure scaffold as a control. For the UV activation experiments, the structures were initially applied at a concentration of 0.1 nM, which is 10-fold lower than in previous assays to account for the expected shift in dynamic range. In the corresponding plaque assays, no PFU were detected for either P-Sc or Sc after UV exposure (Figure 7C). In the absence of UV activation, P-Sc yielded 52% of the PFU obtained with the scaffold alone. For the P-NB

structure, the applied concentration was apparently too low to produce any detectable plaques under either condition. Therefore, in subsequent transformation experiments we used P-NB, NB, and Rod at the original concentration of 1 nM. As expected, in the absence of UV exposure the NB structure yielded only very few PFU, whereas neither the Rod nor the P-NB produced any plaques. After UV activation, however, plaques appeared in the P-NB and NB samples, corresponding to increases to 9% and 0.2% PFU, respectively, relative to the non-irradiated condition. In contrast, the Rod showed no plaque formation with or without UV treatment. (Figure 7C).

When we further tested different UV doses between 300 and 4000 mJ/cm² on the P-NB and NB structures, we occasionally observed extended plaque formation (Figure S10). Given the complexity of the system, we suspect that these effects may, in part, result from additional UV-induced changes, both to the cells and to the underlying DNA origami structures [28], which can influence the level of transformation activation.

To improve the assembly and transformation efficiency after UV cleavage, we designed a dedicated PC construct (P-CSS) in which PC-bridging strands bind at three positions on the CSS and at 36 positions on the origami (Figure 7E and Section S4.1). To determine which component of the P-CSS enters the cell after activation, we used a construct consisting of our HB origami encoding GFP together with a CSSred that carries the same backbone and

antibiotic-resistance cassette as the original scaffold but encodes the red-fluorescent protein DsRed. Successful assembly of the P-CSS construct was confirmed by AGE and TEM imaging (Figure 7F and Section S3.2). UV exposure was applied to the P-CSS, CSSred, and the HB at doses of 0.2, 3.2, and 12.6 J/cm². Agarose gel analysis confirmed the presence of a P-CSS cleavage product, with the amount of cleaved material increasing at higher UV doses (Figure S11). After UV exposure, these structures were used to transform competent *E. coli*.

Bacteria transformed with CSSred showed a reduced transformation efficiency after UV exposure compared to the unexposed control, and red-fluorescent colonies were observed in all cases. Relative values were calculated using the transformation efficiency of CSSred as a reference, which was 1.9×10^8 transformants per nmol. Cells transformed with HB alone displayed negligible transformation efficiency regardless of UV treatment. Whenever colonies appeared, however, they exhibited green fluorescence, as expected. Transformation of *E. coli* with P-CSS resulted in low efficiency in the absence of UV exposure, albeit higher than that of HB, which was likely caused by partial disassembly of the P-CSS during the initial gel cleanup, as observed on the agarose gel (Figure S11). However, a clear increase in transformation efficiency was observed with higher UV exposure, reaching 80% of the CSSred control at the highest UV dose (Figure 7G). 97.5% of the colonies showed red fluorescence, demonstrating that transformation was based on the uptake of the single-stranded scaffold CSSred rather than the origami (Figure S12). Overall, these results demonstrate that UV-induced cleavage of the P-CSS enables controlled release of the circular scaffold from the origami tether, which effectively acts as a “transformation brake”.

3 | Discussion

Our experiments demonstrate that administration of DNA origami structures with gene-encoding scaffolds to *E. coli* and performing a standard heat-shock transformation protocol leads to expression of the encoded genes. The transformation efficiency is, however, considerably reduced compared to the free single-stranded scaffold or plasmids.

While our experiments unequivocally show that the scaffold is somehow taken up by the bacteria, converted into its double-stranded form, and expressed, the details of this process remain unclear. Fluorescence and electron microscopy show that the DNA origami structures localize to the bacterial cell surface, but we were not able to find evidence for DNA origami actually entering the cells. We can speculate about a variety of scenarios for the uptake process, which do not necessarily exclude each other and might, in fact, occur in parallel.

- i) DNA origami enters the cell, where it is disassembled by DNA-binding or DNA-processing enzymes. While we cannot entirely rule out this possibility, it would require the formation of a sufficiently large channel in the cell wall for the origami to enter. Except for the Rod structure (with a diameter of ~4 nm), all origami structures investigated have a minimal extension of ~10 nm in one dimension. A common assumption is that pores formed by heat shock or electroporation are only a few nanometers in size, as such membrane pores must heal quickly enough to prevent cell death by breakdown of the membrane potential. The underlying

peptidoglycan layer is a very dense network with a mesh size too small (2–3 nm) to allow the passage of intact origami structures [34, 35]. Although a few studies of the bacterial cell surface report the presence of larger holes (~10 nm) [36], these did not examine whether the corresponding bacteria were still viable. In any case, transport of an intact origami would require the formation of such a large pore that membrane potential breakdown seems inevitable, making this process rather unlikely. However, it should be noted that even for conventional plasmid transformation by the CaCl₂/heat-shock method, the exact molecular mechanism of DNA uptake has not been fully clarified. Knotted and supercoiled plasmids have dimensions larger (>10 nm) than the maximal peptidoglycan pore sizes (<3.5 nm) reported in *E. coli* [37]. Even the transformation of a fully relaxed, uncoiled plasmid would require a pore size larger than 10 nm because of the curvature radius of DNA helices. While a DNA helix packed around a nucleosome has a diameter of 11 nm, the lower limit of the curvature radius of sterically stressed DNA is 3 nm in highly packed phage capsids [38]. These numbers indicate that the peptidoglycan layer and membrane need to form large nonlethal pores (>10 nm) to allow the passage of intact dsDNA plasmids. It is speculated that this could happen at cell wall-spanning protein machineries [39].

- ii) DNA origami localizes to the bacterial cell surface or outer membrane, and only the single-stranded scaffold is taken up. Due to the high structural flexibility of single-stranded DNA, its uptake is compatible with pore sizes that have been described in *E. coli* (<3.5 nm). In this scenario, flexible parts of an origami—such as exposed single-stranded loops of a partially unfolded structure—would enter the bacterial cell through Nanometer-sized pores generated during heat shock. Once inside, DNA-binding proteins such as SSB or other DNA-processing enzymes could pull in the scaffold strand in a ratcheting process. This process would be less efficient for compact, defect-free structures. Supporting this scenario, we found that the uptake of DNA origami improves for unfolded structures in which increasing numbers of staples are omitted.
- iii) The observed gene expression is driven by contaminants. We cannot exclude that residual scaffold surviving our purification protocol or defective structures are preferentially taken up by the bacteria. We observed that the apparent transformation efficiency is lower for purified samples than for unpurified origami mixtures, pointing toward a contribution of this spurious pathway. However, in the experiments with the PC DNA nanostructures we could observe transformation events only after illumination indicating that residual scaffold is not the main transformation agent.

Considering these points, we assume that both processes ii. and iii. likely play a role. This does not, however, explain the apparent shape dependence of origami transformation—our experiments indicate that the long Rod structure does not lead to any gene expression at all, while the other origami structures investigated lead to expression to varying degrees. In contrast to the 300 nm long Rod, smaller, more compact shapes might enter bacterial cells directly, yet for the reasons outlined above this appears

unlikely. Potentially, certain shapes are better suited for delivering their gene-encoding payload (the scaffold) by providing a larger interaction area with the cell surface. Some shapes may lead to a higher effective concentration of DNA close to the cell membrane upon electrostatic adsorption, and/or present single- or double-stranded protrusions in a way that facilitates uptake. Another possibility is that certain shapes—intricately folded structures and origami blocks with many interior double helices—tend to have larger numbers of defects, rendering their scaffolds more accessible for uptake.

We obtained that polyplex formation with cationic polymers display beneficial effects for the transformation of origami vectors. At low N/P ratios, electrostatic screening likely reduces repulsion between the negatively charged origami and the bacterial cell surface, thereby promoting membrane association [20]. Perhaps polymer-induced diameter reduction further contributes to transformation improvement, as has been reported in other systems [23]. In contrast, increasing N/P ratios progressively suppress *in vitro* formation of the M13 RF, indicating reduced accessibility of the DNA template. Consequently, N/P ratios typically effective in the development of eukaryotic systems are not directly applicable in a bacterial context.

An interesting aspect of our findings is that modification of origami structures with surface-binding AMPs seems to reduce scaffold uptake. This may suggest that the modification “orients” the origami in such a way that the scaffold cannot be accessed or taken up by the cell. An alternative interpretation is that the origami is trapped on the membrane during its passage through the cell envelope. We also utilized the fact that origami folding inhibits transformation rather than promoting it by designing a PC construct that releases a transformable DNA strand upon illumination.

Based on our findings it seems conceivable to realize more sophisticated gene shuttles that are engineered either to prevent DNA from entering the bacterial cell or to controllably release it, potentially by strategically exposing single-stranded sections at specific locations where they can “leak” into the cell and be processed by the cell’s genetic machinery. While such DNA-based nanoconstructs may not improve the overall yield of transformation protocols, they could form the basis of controllable gene-uptake systems for more complex genetic manipulations. We also anticipate that origami structures such as those studied here will ultimately contribute to a more detailed elucidation of bacterial gene-uptake mechanisms, which—particularly in noncompetent bacteria such as *E. coli*—are still not completely understood.

4 | Experimental Section

4.1 | DNA Origami Design

Origamis were designed using caDNAno. Detailed designs and sequences of all structures are provided in Section S4. The HB and the Oct were folded using a 4549-base scaffold. For the coarse-grained representation, the caDNAno json files were imported into oxView. The default force fields used during relaxation were automatically generated by oxView, and a built-in MD relaxation step was executed on GPUs (ox-serve, nanobase.org webserver). After relaxation, an additional short equilibration run was performed in oxView, and the resulting configuration was exported as top and dat files.

4.2 | OxDNA Simulations

MD simulations were carried out using the oxDNA web server [40]. The top and dat files generated in oxView served as input. Simulations were run with the default oxDNA2 model settings provided by the server, using standard temperature and integration parameters. Trajectories were computed on the server-side GPU backend, and the resulting output files were used for subsequent structural analysis.

4.3 | Folding

Folding of DNA origami samples was typically performed by using 100 nm scaffold (in-house produced in 1× TE) combined with a 5× molar excess of staples (IDT) over the scaffold. For the HB and Oct, a folding buffer with 1× TE, 12 mM MgCl₂ and 5 mM NaCl was used. Samples were thermally annealed using a thermal cycling device. After an initial heat up to 95°C for 3 min a thermal annealing ramp was performed from 70°C to 40°C, reducing the temperature by 0.1°C every 2 min.

Folding nanostructures from M13 scaffolds differs only minorly from the protocol above. Assembly of NB, LS, RS and Rod are based on previously established protocols [39]. Assembly of the WF was done as described previously [18]. Because of the asymmetrical nature of this structure, we included further 3D perspectives in Figure S21.

4.4 | Purification and Assembly

Purification was performed in a stepwise manner similar to reference [40]. First PEG precipitation was done. For fluorescence imaging we added the fluorescent dye ATTO647 with a complementary sequence, in 5× excess over the total number of marker extensions. As a last purification step, we performed AGE (60 V, 3 h, 0.5× TBE, 12 mM MgCl₂ running buffer) followed by gel extraction. The structures were extracted based on fluorescence of the added Atto647 marker dye or by ethidium bromide staining.

4.5 | Modification of NB with Biotin and GF-17

For Bt–NB structures, we first assembled the NB after addition of Bt-modified staples in a 10-fold excess. Purification with PEG and AGE verification were done as above. The final structure contains Bt at five positions at the narrow of the NB.

In the second approach, a GF-17/oligonucleotide conjugate was hybridized via bridging strands to poly-T extensions protruding from the NB. After bridging strand and conjugate hybridization steps (1 h agitation RT), intermediates were cleared from unbound DNA strands via PEG purification. The final construct carries GF-17 at ten positions of the wide end of the NB structure. Sequences for both modifications can be found in Table S4.

4.6 | NB Polyplexing with Cationic Polymers

After assembly and PEG purification of the NB structure, linear PEI-25 kDa, and PEI-40 kDa (Kyfora Bio 23966, 24765) and Chitosan (Sigma-Aldrich 523682) were added as described

previously [18]. Multiple polyplexes of different cationic polymer concentrations were made. Coating strength can be defined as N/P , the number of positively charged monomers (number: N) that bind electrostatically to the negatively charged phosphates (number: P) of the DNA backbone. A reference to precise calculations of the N/P values per polymer can be found in the supplements. This structure was used in transformation assays described here and for stability experiments.

4.7 | Isothermal Amplification of NB-Polyplexes

Isothermal amplification was done according to the manufacturer using phi29 DNA Polymerase (Thermo Fisher Scientific, EP0092). Reactions with NB, or NB-polyplexes were prepared omitting primers since origami structure staples are sufficient to prime amplification. After incubation at 37°C for 12 h, the reaction was stopped by inactivating the polymerase at 65°C for 20 min. To quantify the produced M13 DNA, Qubit dsDNA High Sensitivity (Thermo Fisher Scientific, Q33230) was used according to the manufacturer guide. Prediluted samples were measured and quantified using the provided lambda standard.

4.8 | NB Polyplex Stability in *E. coli* Culture Supernatant

First, *E. coli* culture was grown to an exponential growth phase, then filtered through a 0.22 µm PES membrane filter unit. Trapped cells were discarded with the filter and filtrate was used for stability assessment of Polyplex NB variants, naked NB and scaffold. Each DNA structure was incubated at 37°C, 200 rpm, for 1 week. Subsequently structures were analyzed via AGE after decomplexation with 15 mg/mL dextran sulfate (Sigma-Aldrich 42867) in NaOH 0.2 M per 6 nm of NB polyplex. Polyplex formation and decomplexation was done for a minimum of 30 min at RT.

4.9 | Transmission Electron Microscopy

Negative-stain TEM micrographs were recorded using a FEI Tecnai T12 (120 kV) equipped with a Tietz TEMCAM-F416 camera. For negative staining, 1 µL of 5 M NaOH was added to 200 µL of a 2% uranyl formate solution. The staining solution was vortexed for 15 s and subsequently centrifuged for 5 min at 20 000 × g to avoid stain crystals. 5 µL of nanostructure samples were incubated on glow-discharged (Electron Microscopy Sciences, K100X; 20 s, 35 mA, negative polarity) formvar coated carbon Cu400 TEM grids provided by Science Services (München, Germany) and incubated for 30–90 s concentration dependent. Subsequently, the grid was washed with 5 µL of staining solution, incubated with 20 µL staining solution for 30 s if only origami and 15 s if transformed cells with origami were used. Competent *E. coli* cells prepared with Trehalose and CaCl₂ as cryomedium were used to reduce aggregation effects on the grid (Section S1.2). Afterward the grid was dried with filter paper.

4.10 | Fluorescence Microscopy

Images of *E. coli* with labeled origami were taken with an inverted fluorescence microscope (Ti2–2, Nikon, Tokyo,

Japan) equipped with a Digital Sight 50 M Monochrome Microscope Camera and a 100× oil objective (Lambda D 100X Oil CFI Plan Apochrom). The filter cube LED-Cy5-5070A 32 mm was used.

4.11 | Bacterial Strains

Bacteria used in this article for positive selection experiments have been purchased from NEB (NEB 5-alpha Competent *E. coli*) and further processed in our lab. For negative selection experiments, *E. coli* strain XL1-blue competent cells were used. For uptake kinetics *E. coli* BL21 (DE3) strain or “skinny” *E. coli* Δ*min mreB*-A125V was transformed with pMK4.

4.12 | Preparation of Competent Cells

To prepare chemically competent *E. coli* bacteria, an overnight culture in LB medium was cultivated. The next day, 50 mL LB medium was inoculated with the saturated preculture and grown at 37°C at 250 rpm until it reached OD 0.5. Subsequently the culture was incubated on ice for 10 min, followed by a centrifugation step (4°C, 5 min, 2500 × g) to pellet down the bacteria culture. The pellet was dissolved in 15 mL sterile, cold 100 mM CaCl₂ solution and incubated on ice for 20 min. After another centrifugation the pellet was dissolved in 1 mL of the respective transformation buffer. The competent cells were aliquoted and stored at –80°C.

4.13 | Chemical Transformation

Competent *E. coli* bacteria were placed on ice. A volume of 1 µL of 20 nm DNA was added to the competent cells and incubated 30 min. A heat shock at 42°C for 30–60 s followed, then 3 min on ice. For regeneration, 950 µL of SOC medium (SOB + 20 mM Glucose) was added and cells were put in a 37°C shake incubator for a 1 h outgrowth step. For selection, 30 µL of the reaction were plated onto LB-Carbenicillin agar plates.

4.14 | Plaque Assay

For M13-based origami transformation, previously frozen chemically competent *E. coli* (host strain XL-1 blue) was used. On ice, DNA structures were gently mixed with 50 µL of cells to a final concentration of 1 nM. Tubes were then incubated on ice for 30 min and heat shocked at 42°C for 55 s. After 2 min on ice, 125 µL of LB medium was added per tube, and cells were allowed to regenerate for 2.5 h, at 37°C, 250 rpm. For the layer plating, solid LB plates and 0.9% Top Agar were preheated at 37°C and 50°C, respectively. After recovery 4 mL of Top Agar and 50 µL of the reaction were inverted 3–4 times and poured onto warm bottom plates. Before overnight incubation at 37°C, plates were left open for a short period to allow for the top agar to solidify and prevent condensation.

4.15 | Cryo-Electron Tomography (Cryo-ET)

Competent cell stocks were thawed on ice. DNA origami suspension was mixed with 10 nm gold beads blocked with BSA (Sigma-Aldrich,

752584) to a concentration of $\sim 2.5 \times 10^{10}$ particles/ μL . 3 μL of competent cells were gently mixed to 2 μL of ice-chilled origami-gold beads, returned to ice briefly and applied to Quantifoil R2/2200 mesh holey carbon TEM grids (Quantifoil Micro Tools GmbH) in a Vitrobot Mark IV plunge freezer (Thermo Fisher Scientific). Grids were flash vitrified with the following conditions: 95% humidity, 22 C temperature, 10 s wait time, 3 blot force, 10 s blot time. Cryo-ET was performed using a Glacios TEM with Falcon 4 direct electron detector and Selectris energy filter operated with Tomo 5 software (Thermo Fisher Scientific). A total electron flux of 120 e/A^2 was equally distributed across 35 tilt images with a tilt range of $\pm 51^\circ$ with a tilt increment of 3° . Tilt series were preprocessed in RELION 5.0. Motion correction was performed using RELION's implementation of MotionCor2, CTF estimation with CTFFIND4, automated alignment and manual adjustment with IMOD's batchruntomomo and etomo, and tomogram reconstruction with TOMO3D with a SIRT or CTF deconvolution filter. Slice visualization was performed with 3dmod's Slicer.

4.16 | Assembly and UV-Release of Photocleavable P-NB/-Sc Constructs

For the super assembly of the PC-structure, a total of six staple strands were omitted from both NB and Rod. For the assembly of the Rod, these were replaced by six iSpPC PC-bridging strands (IDT), that serve as connectors between the Rod and NB/scaffold (sequences in Table S5). The internal photolabile group can be cleaved via UV 300–350 nm. The P-NB super assembly was prepared by mixing the Rod—bearing the PC linkers—with the NB in equimolar amounts followed by adjustment of the MgCl_2 concentration to 16 mM and overnight incubation at RT in a ThermoMixer (400 rpm). Assembly of the PC-structure was verified via AGE.

All experimental steps involving PC linkers were conducted under red light to prevent premature cleavage. For the UV dependent transformation, 50 μL competent cells were spun down in a PCR tube in a Mini Centrifuge for 30 s. Then 3 μL of 12 nm DNA origami was added on top without mixing. Upon irradiation in UVP Crosslinker (CL-3000) at 365 nm the cells were resuspended and incubated on ice for 30 min, subsequently heat shock transformation was conducted as above. An irradiation dose of 2000 mJ/cm^2 corresponded to an exposure time of approximately 360 s (± 15 s), resulting in an estimated fluence rate of 5.3–5.8 mW/cm^2 .

4.17 | Assembly and UV-Release of Photocleavable P-CSS Constructs

First a PC-linker was designed to be complementary to 24 strands on the HB origami (GFP encoding) and to three binding sites on a dsRed expressing scaffold (CSSred) to increase the binding probability. The PC-linker (IDT, Mod /iSpPC/) was placed next to the CSSred binding side. Then, the PC-linker was hybridized to the CSSred in 10-fold molar excess by incubating at 37°C for 3 h. Subsequently the hybridized CSSred was purified and bound to the HB in threefold molar excess by incubating at 37°C for 3 h. To remove all unbound and higher order combinations, an agarose gel purification was done together with Atto-647 labeled strands bound to the HB origami to be able to precisely

cut out the correct bands. To examine the effect of UV light on the joined constructs (P-CSS), these samples, together with controls consisting of HB and scaffold alone, were exposed to UV from a 300 W xenon light source (Asahi Spectra, MAX-303) equipped with a 365 nm centered bandpass transmission filter. Following this step, the UV exposed samples were transformed as described above.

Author Contributions

V. D., A. H., and M. P. contributed equally to this publication. V. D., F. O., and I. B. contributed to the experiments using negative selection. A. H., M. P., and F. C. S. contributed to the positive selection experiments. V. D., F. O., A. H., M. P., I. B., and F. C. S. conceptualized and planned the research. V. D., A. H., and M. P. performed the experiments. T. R. U. and M. B. recorded and analyzed the Cryo-ET images. F. C. S. and I. B. supervised the project and acquired the funding. V. D., I. B., A. H., M. P., and F. C. S. contributed to the writing process. All authors discussed the scientific results.

Acknowledgments

The authors thank Sofia Ruiz Rodriguez and Yasaman Ahmadi for their help with origami folding, purification, and agarose gel electrophoresis of HB, Oct, and NB (polyplex) nanostructures. The authors thank Dr. Simone Stegbauer for her help with the measurement of the UV irradiation spectrum. Figures were partly created in BioRender. Ponetsmüller, M (2026) <https://BioRender.com/8i9o759> & <https://BioRender.com/3axbzy>. This project has received funding from the Horizon Europe – EIC Pathfinder Challenges program under agreement no. 101115215 and from the Deutsche Forschungsgemeinschaft (DFG SI 761/6-1) under the project no. 468955252.

Open Access funding provided by Austrian Institute of Technology GmbH/KEMÖ.

Funding

This study was supported by Horizon Europe – EIC Pathfinder Challenges Program (Grant 101115215) and Deutsche Forschungsgemeinschaft (DFG SI 761/6-1, Project 468955252).

Conflicts of Interest

The authors declare no conflicts of interest.

Data Availability Statement

Data are available from the corresponding author, upon request.

References

1. S. M. Douglas, H. Dietz, T. Liedl, et al., "Self-Assembly of DNA into Nanoscale Three-Dimensional Shapes," *Nature* 459 (2009): 414–418, <https://doi.org/10.1038/nature08016>.
2. P. W. K. Rothmund, "Folding DNA to Create Nanoscale Shapes and Patterns," *Nature* 440 (2006): 297–302, <https://doi.org/10.1038/nature04586>.
3. X. Wu, C. Yang, H. Wang, et al., "Genetically Encoded DNA Origami for Gene Therapy In Vivo," *Journal of the American Chemical Society* 145 (2023): 9343–9353, <https://doi.org/10.1021/JACS.3C02756>.
4. C. Yang, J. Fan, H. Zhu, et al., "Genetically Encoded Nucleic Acid Nanostructures for Biological Applications," *ChemBioChem* 26 (2025): e202400991, <https://doi.org/10.1002/CBIC.202400991>.
5. Y. Xu, Y. Yang, Q. Shi, et al., "An Infectious Virus-Like Particle Built on a Programmable Icosahedral DNA Framework," *Angewandte* 2022, <https://doi.org/10.1002/anie.202214731>.

6. J. A. Garcia-Diosa, G. Grundmeier, and A. Keller, "Effect of DNA Origami Nanostructures on Bacterial Growth," *ChemBioChem* 25 (2024): e202400091, <https://doi.org/10.1002/cbic.202400091>.
7. Y. Ahmadi, T. R. Umrekar, N. Mutter, et al., "DNA Origami-Enhanced Binding of Aptamers to Staphylococcus Aureus Cells," *Biosensors and Bioelectronics: X* 16 (2024): 100436, <https://doi.org/10.1016/j.biosx.2023.100436>.
8. Ö Coşkuner Leineweber, B. K. Pothineni, N. Schumann, et al., "Vancomycin-Modified DNA Origami Nanostructures for Targeting Bacterial Pathogens," *Small Structures* 6 (2025): 2500246, <https://doi.org/10.1002/ssr.202500246>.
9. Y. Hao, Q. Li, C. Fan, et al., "Data Storage Based on DNA," *Small Structures* 2 (2021): 2000046, <https://doi.org/10.1002/ssr.202000046>.
10. L. Tang, Z. Tian, J. Cheng, et al., "Circular Single-Stranded DNA as Switchable Vector for Gene Expression in Mammalian Cells," *Nature Communications* 14 (2023): 6665, <https://doi.org/10.1038/s41467-023-42437-6>.
11. J. A. Kretzmann, A. Liedl, A. Monferrer, et al., "Gene-Encoding DNA Origami for Mammalian Cell Expression," *Nature Communications* 14 (2023): 1017, <https://doi.org/10.1038/s41467-023-36601-1>.
12. Z. Tian, D. Shao, L. Tang, et al., "Circular Single-Stranded DNA as a Programmable Vector for Gene Regulation in Cell-Free Protein Expression Systems," *Nature Communications* 15 (2024): 4635, <https://doi.org/10.1038/s41467-024-49021-6>.
13. I. Seitz, S. Saarinen, J. Wierzchowicka, et al., "Folding of mRNA-DNA Origami for Controlled Translation and Viral Vector Packaging," *Advanced Materials* 37 (2025): 2417642, <https://doi.org/10.1002/ADMA.202417642>.
14. M. Hu, C. Feng, Q. Yuan, et al., "Lantern-Shaped Flexible RNA Origami for Smad4 mRNA Delivery and Growth Suppression of Colorectal Cancer," *Nature Communications* 14, no. 1 (2023): 1307, <https://doi.org/10.1038/s41467-023-37020-y>.
15. J. R. Walker and E. Altman, "Biotinylation Facilitates the Uptake of Large Peptides by Escherichia Coli and Other Gram-Negative Bacteria," *Applied and Environmental Microbiology* 71 (2005): 1850, <https://doi.org/10.1128/AEM.71.4.1850-1855.2005>.
16. F. Bottari, E. Daems, A. M. De Vries, et al., "Do Aptamers Always Bind? The Need for a Multifaceted Analytical Approach When Demonstrating Binding Affinity between Aptamer and Low Molecular Weight Compounds," *Journal of the American Chemical Society* 142 (2020): 19622–19630, <https://doi.org/10.1021/JACS.0C08691>.
17. V. Linko and A. Keller, "Stability of DNA Origami Nanostructures in Physiological Media: The Role of Molecular Interactions," *Small* 19 (2023): 2301935, <https://doi.org/10.1002/smll.202301935>.
18. Y. Ahmadi, E. De Llano, and I. Barišić, "(Poly)cation-Induced Protection of Conventional and Wireframe DNA Origami Nanostructures," *Nanoscale* 10 (2018): 7494–7504, <https://doi.org/10.1039/c7nr09461b>.
19. J. K. Kiviahio, V. Linko, A. Ora, et al., "Cationic Polymers for DNA Origami Coating – Examining Their Binding Efficiency and Tuning the Enzymatic Reaction Rates," *Nanoscale* 8 (2016): 11674–11680, <https://doi.org/10.1039/C5NR08355A>.
20. N. Ponnuswamy, M. M. C. Bastings, B. Nathwani, et al., "Oligolysine-Based Coating Protects DNA Nanostructures from Low-Salt Denaturation and Nuclease Degradation," *Nature Communications* 8 (2017): 15654, <https://doi.org/10.1038/ncomms15654>.
21. H. Bila, E. E. Kurisinkal, and M. M. C. Bastings, "Engineering a Stable Future for DNA-Origami as a Biomaterial," *Biomaterials Science* 7 (2019): 532–541, <https://doi.org/10.1039/C8BM01249K>.
22. A. Chopra, S. Krishnan, and F. C. Simmel, "Electrotransfection of Polyamine Folded DNA Origami Structures," *Nano Letters* 16 (2016): 6683–6690, <https://doi.org/10.1021/acs.nanolett.6b03586>.
23. D. W. Pack, A. S. Hoffman, S. Pun, et al., "Design and Development of Polymers for Gene Delivery," *Nature Reviews Drug Discovery* 4, no. 7 (2005): 581–593, <https://doi.org/10.1038/nrd1775>.
24. S. Mao, W. Sun, and T. Kissel, "Chitosan-Based Formulations for Delivery of DNA and siRNA," *Advanced Drug Delivery Reviews* 62 (2010): 12–27, <https://doi.org/10.1016/J.ADDR.2009.08.004>.
25. N. Saranya, A. Moorthi, S. Saravanan, et al., "Chitosan and Its Derivatives for Gene Delivery," *International Journal of Biological Macromolecules* 48 (2011): 234–238, <https://doi.org/10.1016/j.ijbiomac.2010.11.013>.
26. U. Lungwitz, M. Breunig, T. Blunk, et al., "Polyethylenimine-Based Non-Viral Gene Delivery Systems," *European Journal of Pharmaceutics and Biopharmaceutics* 60 (2005): 247–266, <https://doi.org/10.1016/j.ejpb.2004.11.011>.
27. S. M. Douglas, A. H. Marblestone, S. Teerapittayanon, et al., "Rapid Prototyping of 3D DNA-Origami Shapes with caDNAno," *Nucleic Acids Research* 37 (2009): 5001–5006, <https://doi.org/10.1093/nar/gkp436>.
28. H. Jun, X. Wang, M. F. Parsons, et al., "Rapid Prototyping of Arbitrary 2D and 3D Wireframe DNA Origami," *Nucleic Acids Research* 49 (2021): 10265–10274, <https://doi.org/10.1093/nar/gkab762>.
29. R. Veneziano, S. Ratanalert, K. Zhang, et al., "Designer Nanoscale DNA Assemblies Programmed from the Top down," *Science* 352 (2016): 1534, <https://doi.org/10.1126/SCIENCE.AAF4388>.
30. D. Kufák, L. Melo, F. Schroeder, et al., "CATANA: An Online Modelling Environment for Proteins and Nucleic Acid Nanostructures," *Nucleic Acids Research* 50 (2022): W152–W158, <https://doi.org/10.1093/nar/gkac350>.
31. Y. Ahmadi, F. Savini, N. Mutter, et al., "Application of Antimicrobial Peptides as Diagnostic Biosensors," *Analytical Chemistry* 96 (2023): 256–264, <https://doi.org/10.1021/ACS.ANALCHEM.3C03854>.
32. P. Demchick and A. L. Koch, "The Permeability of the Wall Fabric of Escherichia Coli and Bacillus Subtilis," *Journal of Bacteriology* 178 (1996): 768–773, <https://doi.org/10.1128/JB.178.3.768-773.1996>.
33. N. Vázquez-Laslop, H. Lee, R. Hu, et al., "Molecular Sieve Mechanism of Selective Release of Cytoplasmic Proteins by Osmotically Shocked Escherichia Coli," *Journal of Bacteriology* 183 (2001): 2399, <https://doi.org/10.1128/JB.183.8.2399-2404.2001>.
34. R. D. Turner, A. F. Hurd, A. Cadby, et al., "Cell Wall Elongation Mode in Gram-Negative Bacteria Is Determined by Peptidoglycan Architecture," *Nature Communications* 4, no. 1 (2013): 1496, <https://doi.org/10.1038/ncomms2503>.
35. J. C. Gumbart, M. Beeby, G. J. Jensen, et al., "Escherichia Coli Peptidoglycan Structure and Mechanics as Predicted by Atomic-Scale Simulations," *PLoS Computational Biology* 10 (2014): e1003475, <https://doi.org/10.1371/JOURNAL.PCBI.1003475>.
36. H. G. Garcia, P. Grayson, L. Han, et al., "Biological Consequences of Tightly Bent DNA: The Other Life of a Macromolecular Celebrity," *Biopolymers* 85 (2007): 115–130, <https://doi.org/10.1002/BIP.20627>.
37. E. M. Scheurwater and L. L. Burrows, "Maintaining Network Security: How Macromolecular Structures Cross the Peptidoglycan Layer," *FEMS Microbiology Letters* 318 (2011): 1–9, <https://doi.org/10.1111/J.1574-6968.2011.02228.X>.
38. E. Poppleton, R. Romero, A. Mallya, et al., "OxDNA.org: A Public Webserver for Coarse-Grained Simulations of DNA and RNA Nanostructures," *Nucleic Acids Research* 49 (2021): W491–W498, <https://doi.org/10.1093/NAR/GKAB324>.
39. Y. Ahmadi, A. L. Nord, A. J. Wilson, et al., "The Brownian and Flow-Driven Rotational Dynamics of a Multicomponent DNA Origami-Based Rotor," *Small* 16 (2020): 2001855, <https://doi.org/10.1002/SMLL.202001855>.

40. K. F. Wagenbauer, F. A. S. Engelhardt, E. Stahl, et al., "How We Make DNA Origami," *ChemBioChem* 18 (2017): 1873–1885, <https://doi.org/10.1002/CBIC.201700377>.

Supporting Information

Additional supporting information can be found online in the Supporting Information section. **Supporting Fig. S1:** Agarose gel image of folded HB, folded Oct and scaffold strand (CSS). Bands marked in pink have been excised from gel. **Supporting Fig. S2:** Transformation efficiency of chemically competent *E. coli* as a function of cryopreservation medium and DNA origami purification method. Relative transformation efficiency (CFU, %) is shown for circular scaffold DNA (CSS) and for HB and Oct DNA origami prepared either by gel purification or PEG precipitation. Competent cells were generated using glycerol-containing CaCl₂ buffer, trehalose-containing CaCl₂ buffer, or CaCl₂-only buffer. All values are normalized to the transformation efficiency of CSS in glycerol-containing buffer (first bar, set to 100%). Competent cells prepared in glycerol-containing CaCl₂ buffer showed higher transformation efficiencies than trehalose-preserved and CaCl₂-only cells. For both HB and Oct structures, PEG-purified samples consistently exhibited higher transformation efficiencies than gel-purified counterparts, indicating a significant influence of purification method on transformation performance. Error bars represent standard deviation. Data is based on n=7 independent measurements for CSS and HB gel-purified (Glycerol and Trehalose), all other samples were recorded with a sample size of n=3 independent measurements. All transformations were performed under identical DNA input and cell number conditions. **Supporting Fig. S3:** Agarose gel image of folded HB, folded Oct and scaffold strand (CSS) in different media. In origami folding buffer (FOB12.5), in competent cell medium with 10% Glycerol (in Glyc.) and in competent cell medium with 300 mM Trehalose (in Treh.). **Supporting Fig. S4:** Agarose gel image of scaffold strand (CSS), folded HB origami and folded undersaturated variants of the origami with 75% (75% -HB), 50% (50% -HB), or 25% (25% -HB) of the total staple strands. Bands marked with a pink rectangle contain the correctly folded origami structures and are cut from the gel. **Supporting Fig. S5:** TEM micrographs of deliberately underfolded HB origami structures. Origami folding was performed using A) 75%, B) 50%, and C) 25% of the total staple set. Corresponding structures folded with the indicated fractions of staples were simulated using oxDNA (Figure 3A). The oxDNA simulations represent ensemble-averaged mean conformations characterized by a root-mean-square deviation (RMSD); thus, the depicted structures reflect average configurations rather than experimentally verified static states, with higher RMSD values indicating increased conformational variability. HB origami folded with 75% staples exhibit well-defined structures in TEM that are in good agreement with the simulation results. HB origami folded with 50% staples are already difficult to identify, and samples folded with 25% staples show no discernible origami structures beyond densely clustered DNA. Owing to the increased conformational flexibility expected for these loosely folded assemblies, their structural features cannot be reliably resolved by TEM imaging. Scale bar: 100 nm. **Supporting Fig. S6:** Transformation of scaffold (Sc) variants 7249-nt, 7560-nt, and 8064-nt after 2.5 and 5 h of regeneration. PFU were calculated relative to Sc 7249-nt 5h and are depicted with respective standard deviations. Variants show different levels of phage production independent of the sequence length. **Supporting Fig. S7:** Effect of polycationic coating on NB origami stability in *E. coli* culture supernatant. Agarose gel electrophoresis images are shown. Bands 1–4 show Scaffold (ScNB) and noncoated NB (NB) incubated 1 week in storage buffer and *E. coli* culture supernatant (EcSN). Bands 5–9 and 10–14 show EcSN stability of NB coated with different N/P concentrations of PEI-25 kDa and PEI-40 kDa (NB 8-0.03), respectively. Before application to the gel, cationic polymers and NB were decomplexed via dextran sulfate (DS) to enable migration. Decomplexing failed in one sample with the highest concentration of PEI-40 (N/P 8 band 10). At the DS step equivalent stability tests with chitosan failed since most of the samples remained in the pocket (not depicted). Lane 5, 6, 11 with high N/P do not show smearing below bands. Without polymers and with decreasing N/P smears appear as sign of beginning instability. Under storage buffer control conditions, bands remain stable and sharp.

Supporting Fig. S8: Cryo-ET Images of XL-1 blue cells and DNA origami. (A) Native cells with NB, (B) competent cells with NB, and (C) competent cells with NB PEI25 N/P 0.1 polyplex. Samples were imaged right after the heat shock step of the optimized transformation protocol. DNA origamis are annotated with blue stars. Images without Origami are shown as well for they nicely depict differences between native and competent cells. Chemically competent XL-1 blue cells show outer membrane deformations and invaginations. Images depict numerous events of the DNA origami being closely associated with the outer membrane for both polyplex-, and single NB. There are some images that potentially show DNA origami passing through the outer membrane or residing in the periplasm—but this is not certain (B and C). Native cells didn't show membrane deformations or nearby DNA origami in this. **Supporting Fig. S9:** Agarose gel electrophoresis of P-NB photocleavage. DNA samples in storage buffer (OB), and transformation buffer (100 mM CaCl₂) are depicted next to each other. Structures used to assemble were loaded from lane 1–8. P-NB exposed with 150 mJ/cm²–20 J/cm² UV dosages and a no UV control samples were loaded from 9–18. Without UV the DNA structures, migrated expected distances (lane 2, 4, 6, 8, and 10) with only slight retardation due to CaCl₂ (lane 5, 7, 9). Scaffolds in CaCl₂ containing buffer stayed inside of the pocket (lane 1,3). P-NB cleavage can be seen where bands shift from ~3 kb to the level of the separated components (NB, Rod) at ~1.5 kb after UV exposure. Cleavage can be confirmed confidently starting from 1000 mJ/cm² (lane 11–14) below this threshold cleavage appears to be insufficient (lane 15–18). **Supporting Fig. S10:** Transformation of P-NB with and without UV exposure from 300–4000 mJ/cm². Layer agar plates with PFU are depicted. No plaques were formed without UV or 300 mJ/cm² exposure. PFU only started to appear from 2000 mJ/cm² and increased further in 4000 mJ/cm². Due to extensive plaque formation, % confluency was used to compare transformation efficiency. **Supporting Fig. S11:** Agarose gel image of photocleavage experiment. Left: scaffold strand (CSSred) with attached PC-linker, folded HB origami and combined construct of CSSred and HB joined together with the photolinker (P-CSS) without UV radiation. Right: P-CSS construct after 1 min (0.2 J/cm²), 15 min (3.2 J/cm²) and 60 min (12.6 J/cm²) UV radiation. The disassembly of the linked construct is shown by decreasing intensity of the P-CSS band, while the single bands at the height of CSS and HB are increasing in intensity. **Supporting Fig. S12:** Images of transformation plates for DH5a bacteria, that have been transformed with the joint construct P-CSS. Images in Cy2 and Cy3 channel have been acquired with an Amersham Typhoon laser scanner and the following settings: Cy2: Laser 488 nm, Filter: Cy2 525BP20 (515-535 nm), Cy3: Laser 532 nm, Filter: Cy3 570BP20 (560-580 nm). Images in the last row have been acquired using a transilluminator with a blue LED and an orange filter. Bacteria colonies, which have taken up the C_{ss}Red DNA during transformation have a high intensity with the Cy3 settings, while bacteria that have taken up the HB origami scaffold sequence display green fluorescence, as can be seen in the Cy2 channel and the transilluminator image in the last row. Fraction of red colonies on the plates: 0 J/cm²: 93.8%, 0.42 J/cm²: 95.8%, 3.2 J/cm²: 96.7%, 12.6 J/cm²: 97.5%. **Supporting Fig. S13:** Fotos of viability control layer plates of *E. coli* treated under UV experimental conditions. UV 302 nm exposed cells in layer plates show decreased viability already in 2000 mJ/cm² samples (no growth zones within layer) compared to the no UV control and 365 nm UV samples (evenly distributed cells). Mean values ± SD were calculated (n = 2 technical replicates). **Supporting Fig. S14:** Fotos of viability control streak plates of *E. coli* treated under UV experimental conditions. UV 365 nm exposed cells show decrease of CFU formation with 2000 mJ/cm² (75% ± 27% of no UV control) and 10000 mJ/cm² (48% ± 14% of no UV control). Mean values ± SD were calculated (n=2 technical replicates). **Supporting Fig. S15:** Scaffold routing and staple design for HB origami. Scaffold routing is shown in blue, GFP gene-encoding sequence in green, staples with handle sequences for fluorescent dye and/or scaffold (CSSred) attachment in red(if needed) and all other staples in gray. CaDNAno version 2.4 was used for design. **Supporting Fig. S16:** Scaffold routing and staple design for Oct origami. Scaffold routing is shown in blue, GFP gene-encoding sequence in green, staples in gray. CaDNAno version 2.4 was used for design. **Supporting Fig. S17:** Scaffold routing and staple design for HB origami with 75% staples of the whole staple set. Scaffold routing is shown in blue, GFP

gene-encoding sequence in green, staples in gray. CaDNAno version 2.4 was used for design. **Supporting Fig. S18:** Scaffold routing and staple design for HB origami with 50 % staples of the whole staple set. Scaffold routing is shown in blue, GFP gene encoding sequence in green, staples in gray. CaDNAno version 2.4 was used for design. **Supporting Fig. S19:** Scaffold routing and staple design for HB origami with 50 % staples of the whole staple set. Scaffold routing is shown in blue, GFP gene encoding sequence in green, staples in gray. CaDNAno version 2.4 was used for design. **Supporting Fig. S20:** Representative agarose gel electrophoresis of M13-based DNA origamis. Scaffolds variants with 8064-nt, 7560-nt, and 7249-nt were loaded flanking their respective DNA origami structures (Rod, LS; RS, WF; NB). For each origami structure crude (C), PEG-purified (P) and supernatant (SN) was verified. All DNA origami structures appear at respective sizes (migrating slower than scaffolds) without additional multimeric structures (bands of higher molecular weight). Staples appear faintly as low bands (<0.25 kb) in crude samples and disappear with purification. Supernatant (PEG buffer) was loaded to assess loss of material during purification. No bands indicate efficient retrieval of the origami structures. **Supporting Fig. S21:** Monomeric 3D structures of the WF origami illustrated with CATANA. The model was rotated twice at 45° around the horizontal axis from the front (left) to the lateral view (right), as indicated by curved arrows. **Supporting Table S1:** Systematic reduction of key steps of the standard heat-shock transformation protocol. Plasmid pMK4 was used to transform *E. coli* with alternating conditions (column C1). Incubation time on ice before heat shock (C2), reaction cell volume (C3), and time/temperature of heat shock (C4) were compared. CFU/ml of positive transformants and respective values per second are depicted incl. standard deviation. **Supporting Table S2:** Staple sequence for HB Sequences in red are added in case of fluorescent dye attachment and/or scaffold (CSSred) attachment. **Supporting Table S3:** Staple sequence for Oct. **Supporting Table S4:** Staple sequence for 75 % staples of HB. **Supporting Table S5:** Staple sequence for 50 % staples of HB. **Supporting Table S6:** Staple sequence for 25 % staples of HB. **Supporting Table S7:** Biotin and AMP Staples for modified NB. **Supporting Table S8:** Photocleavable staples for P-structures.